Earth and Planetary Science Letters 447 (2016) 72–83

Contents lists available at ScienceDirect

Earth and Planetary Science Letters

www.elsevier.com/locate/epsl

Temperature of Earth's core constrained from melting of Fe and $Fe_{0.9}Ni_{0.1}$ at high pressures

Dongzhou Zhang [a,b,c,*], Jennifer M. Jackson [a], Jiyong Zhao [b], Wolfgang Sturhahn [a], E. Ercan Alp [b], Michael Y. Hu [b], Thomas S. Toellner [b], Caitlin A. Murphy [d], Vitali B. Prakapenka [e]

[a] Seismological Laboratory, California Institute of Technology, 1200 E California Blvd, MS 252-21, Pasadena, CA 91125, USA
[b] Advanced Photon Source, Argonne National Laboratory, 9700 S Cass Ave, Argonne, IL 60439, USA
[c] Hawaii Institute of Geophysics and Planetology, University of Hawaii at Manoa, Honolulu, HI 96822, USA
[d] AAAS Science & Technology Policy Fellow, United States Department of Energy, 1000 Independence Avenue SW, Washington, DC 20585, USA [1]
[e] GSECARS, University of Chicago, 9700 S Cass Ave, Argonne, IL 60439, USA

ARTICLE INFO

Article history:
Received 22 December 2015
Received in revised form 24 April 2016
Accepted 26 April 2016
Available online 12 May 2016
Editor: J. Brodholt

Keywords:
Fe
Fe–Ni
melting
core
high pressure

ABSTRACT

The melting points of *fcc*- and *hcp*-structured $Fe_{0.9}Ni_{0.1}$ and Fe are measured up to 125 GPa using laser heated diamond anvil cells, synchrotron Mössbauer spectroscopy, and a recently developed fast temperature readout spectrometer. The onset of melting is detected by a characteristic drop in the time-integrated synchrotron Mössbauer signal which is sensitive to atomic motion. The thermal pressure experienced by the samples is constrained by X-ray diffraction measurements under high pressures and temperatures. The obtained best-fit melting curves of *fcc*-structured Fe and $Fe_{0.9}Ni_{0.1}$ fall within the wide region bounded by previous studies. We are able to derive the γ–ϵ–l triple point of Fe and the quasi triple point of $Fe_{0.9}Ni_{0.1}$ to be 110 ± 5 GPa, 3345 ± 120 K and 116 ± 5 GPa, 3260 ± 120 K, respectively. The measured melting temperatures of Fe at similar pressure are slightly higher than those of $Fe_{0.9}Ni_{0.1}$ while their one sigma uncertainties overlap. Using previously measured phonon density of states of *hcp*-Fe, we calculate melting curves of *hcp*-structured Fe and $Fe_{0.9}Ni_{0.1}$ using our (quasi) triple points as anchors. The extrapolated $Fe_{0.9}Ni_{0.1}$ melting curve provides an estimate for the upper bound of Earth's inner core–outer core boundary temperature of 5500 ± 200 K. The temperature within the liquid outer core is then approximated with an adiabatic model, which constrains the upper bound of the temperature at the core side of the core–mantle boundary to be 4000 ± 200 K. We discuss a potential melting point depression caused by light elements and the implications of the presented core–mantle boundary temperature bounds on phase relations in the lowermost part of the mantle.

1. Introduction

Cosmochemical and seismological studies suggest that Earth's core is primarily composed of iron with ~5 wt% nickel, plus ~10 wt% light elements, such as sulfur, oxygen, silicon and carbon (McDonough and Sun, 1995; Li and Fei, 2003; Hirose et al., 2013). The core consists of a solid inner section surrounded by a convecting, liquid outer layer (Lehmann, 1936; Deuss, 2014). Experiments show that the inclusion of light elements tends to lower the melting point of Fe-rich alloys (e.g., Boehler, 1992; Fei and Bertka, 2005; Stewart et al., 2007; Chen et al., 2008; Andrault et al., 2009; Asanuma et al., 2010; Terasaki et al., 2011, and references therein). The melting temperatures of pure iron and iron alloyed with a few percent nickel therefore provide the basis for understanding expected temperatures in the core. The temperature of the core at the core–mantle boundary (CMB) provides constraints on the heat flow across this boundary and thus affects the age determination of the inner core (Labrosse et al., 2001), influences the evolution of the geodynamo (Olson, 2013), and controls the temperature gradient within the thermal boundary layer above the CMB (Anderson, 1990; Lay et al., 2008).

Among the four crystalline forms of Fe, the high-pressure phases face-centered cubic (*fcc*) and hexagonal close packed (*hcp*) are the primary focus of this study. The melting curve of *fcc* Fe constrains the *fcc*–*hcp*-liquid (γ–ϵ–l) triple point, an essential reference point for the melting curve of the *hcp* phase under

* Correspondence to: Hawaii Institute of Geophysics and Planetology, University of Hawaii at Manoa, Honolulu, HI 96822, USA.
E-mail address: dzhang@hawaii.edu (D. Zhang).
[1] Current address.

http://dx.doi.org/10.1016/j.epsl.2016.04.026
0012-821X/

large compression. However, the high pressure melting curves of *fcc*- and *hcp*-Fe are still controversial, leading to estimated temperatures at the inner core–outer core boundary ranging from 4850 K to 7800 K (Williams et al., 1987; Boehler et al., 1990; Shen et al., 1998; Jackson et al., 2013; Anzellini et al., 2013; Aquilanti et al., 2015). In particular, studies of the high pressure melting curve of *fcc*- and *hcp*-Fe–Ni alloys are not available.

Several experimental methods have been used to explore the high pressure melting curves of metals, among which the laser heated diamond anvil cell (LH-DAC) is the most common (e.g., Boehler, 1993; Errandonea et al., 2001; Shen et al., 2004; Dewaele et al., 2007, 2010; Jackson et al., 2013; Anzellini et al., 2013; Zhang et al., 2015). In LH-DAC experiments, the temperature determination is usually less accurate and precise than the pressure determination. Major contributions to the temperature uncertainty in LH-DAC experiments are rapid temporal fluctuations (10–100 Hz) of the sample temperature during the experiment (Jeanloz and Heinz, 1984; Zhang et al., 2015). These fluctuations are likely a result of the coupling between laser light and sample surface, and at temperatures close to a sample's melting point ~0.3% of laser power fluctuation can lead to temperature fluctuations of up to 200 K (Jeanloz and Heinz, 1984; Jeanloz and Kavner, 1996). Also, slower (1 Hz) temperature fluctuations of several hundreds of Kelvin have been reported for samples near their melting points (Dewaele et al., 2007, 2010; Anzellini et al., 2013; Zhang et al., 2015). This magnitude of temperature fluctuation presents a challenge for accurately and precisely determining the melting temperature of a sample.

Melting experiments in a LH-DAC typically ramp up the laser power quickly (seconds to minutes) to convert the sample from solid to liquid. Therefore, a fast temperature readout system whose sampling frequency exceeds that of the melting diagnostic is necessary to obtain reliable sample temperatures with high precision. We have developed a multi-wavelength temperature readout spectrometer named FasTeR to address this issue (Zhang et al., 2015). The FasTeR system features a well-calibrated sampling rate of 100 Hz (and up to at least 400 Hz) with large dynamic range, high sensitivity, and a well-constrained optical aperture. This new system is located at beamline 3-ID-B of the Advanced Photon Source (APS) at Argonne National Laboratory, IL and described in detail elsewhere (Zhang et al., 2015).

In this study, we combine the LH-DAC, the FasTeR spectrometer, and synchrotron Mössbauer spectroscopy to constrain the high pressure melting curves of *fcc*- and *hcp*-structured $^{57}Fe_{0.9}Ni_{0.1}$ and ^{57}Fe up to pressures of 125 GPa. The Mössbauer signal that scatters from the sample prior to melting is sensitive to the movement of the iron nuclei (Singwi and Sjölander, 1960; Boyle et al., 1961), and thus provides a unique diagnostic for the solid–liquid transition of Fe-rich materials (Jackson et al., 2013).

2. Experiments

2.1. Sample preparation

The Fe–Ni sample used in this study was synthesized at Caltech. Individual pieces of Ni and 95%-enriched ^{57}Fe are selected with an accuracy of 1.0 mg to produce 50 mg of $Fe_{0.9}Ni_{0.1}$. The Fe and Ni pieces are arc-melted in an argon atmosphere, then cold rolled to a physical thickness of about 13 μm. The elemental composition of the Fe–Ni sample is determined by a JEOL JXA-8200 electron probe micro-analyzer (EPMA) at Caltech's Microanalysis Center. Quantitative data are acquired in focused mode, using wavelength-dispersive spectrometry, operating at 15 kV accelerating voltage and 20 nA beam current. Pure Fe, Ni and Re metal standards are used for the analysis. No elements other than Fe and Ni are detected within the uncertainty. EPMA analysis of 25 sampled regions gives an average composition of $Fe_{0.91(1)}Ni_{0.09(1)}$ for the ^{57}Fe–Ni alloy, where the numbers in parentheses indicate the uncertainties in the last digit, hereafter referred to as $Fe_{0.9}Ni_{0.1}$ for simplicity. The 95% isotopically enriched ^{57}Fe and $Fe_{0.9}Ni_{0.1}$ foils with thicknesses ranging from 9 to 15 μm are cut into rectangular sections with an EDM and cleaned. The sizes of the sections range from about 55×55 μm^2 to 80×80 μm^2. The ^{57}Fe samples used in this study are cut from the same larger foils used in a previous melting study (Jackson et al., 2013).

In each melting run, a symmetric DAC is used to provide the high pressure environment. Two quarter-carat Type-I diamonds with culet sizes ranging from beveled 250 to 300 μm in diameter are mounted on backing plates (WC or cBN) and aligned to form the anvils. A Re gasket is pre-indented to ~45 μm thickness, and to form the sample chamber, a hole is drilled in the center of the pre-indentation using an EDM or a laser drilling system. The sample chamber's size ranges from 80 to 115 μm in diameter, depending on the diamond culet size. Dehydrated KCl is pressed into transparent flakes and loaded together with an individual pre-cut $^{57}Fe_{0.9}Ni_{0.1}$ or ^{57}Fe foil in a sandwich configuration into the sample chamber. The KCl serves as both a pressure-transmitting medium and thermal insulation. A few ruby spheres (~10 μm in diameter) are placed away from the sample and used as pressure markers (Mao et al., 1986). The DAC is first purged in a chamber filled with purified Ar gas and then heated in a vacuum furnace before closing to remove oxygen and moisture. After the DAC is sealed, pressure is increased to the approximate desired range and laser annealed to about 1500 K before the X-ray experiments. The laser annealing is essential to determine sample coupling behavior with the IR laser and to relax any stresses induced by cold compression. When possible, X-ray diffraction is collected *in-situ* to constrain the pressure of the sample.

2.2. Synchrotron Mössbauer spectroscopy measurements

The dynamics of the iron atoms are used as a diagnostic to detect melting and are probed using nuclear resonant forward scattering, also known as synchrotron Mössbauer spectroscopy (SMS) (Jackson et al., 2013). As explained previously, the observed time-delayed signal is caused by coherent elastic scattering of synchrotron X-rays while traversing a sample containing ^{57}Fe or another accessible nuclear resonant isotope (Jackson et al., 2013). The emission of the SMS signal occurs into the direction of the incident X-rays and is independent of the spatial positions of atoms. The strength of the SMS signal is primarily determined by the effective thickness of the sample traversed by the X-rays. The effective thickness, η, is a dimensionless number given as the product of the numerical density of the ^{57}Fe nuclei, ρ, the physical thickness of the sample, d, the nuclear resonant cross section, $\sigma = 2.56 \times 10^{-22}$ m^2 for ^{57}Fe, and the dimensionless temperature-dependent Lamb–Mössbauer factor, f

$$\eta = \rho\, d\, \sigma\, f \quad . \tag{1}$$

The experiments are carried out at beamline 3-ID-B of the APS, which uniquely features nuclear resonant scattering techniques coupled with *in-situ* double-sided laser heating, a new FasTeR temperature measurement system, conventional CCD-based spectrometers, and X-ray diffraction (Zhao et al., 2004; Gao et al., 2009; Jackson et al., 2013; Zhang et al., 2015). The storage ring is operated in low-emittance top-up mode with 24 bunches that are separated by 153 ns. The energy (14.4125 keV) and resolution (1 meV) of the X-rays are determined by a silicon high resolution monochromator (Toellner, 2000), and a focus area of $\sim 10 \times 11$ μm^2 (full width at half maximum) is achieved by a Kirkpatrick–Baez mirror system (Eng et al., 1998; Zhang et al., 2015). *In-situ* X-ray diffraction images are collected on the compressed samples at the

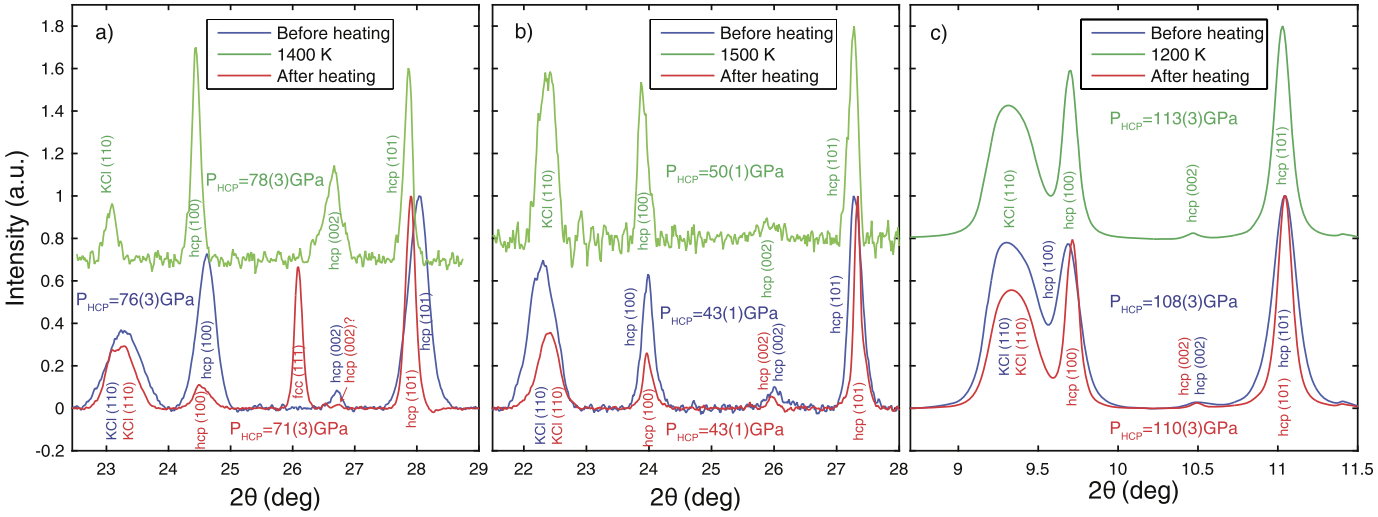

Fig. 1. X-ray diffraction patterns collected before (300 K, blue), during (green) and after (300 K, red) typical melting runs. Panels (a), (c) and (b) show results for $Fe_{0.9}Ni_{0.1}$ and Fe, respectively. Diffraction patterns in panels (a) and (b) are collected at APS 3-ID-B with an X-ray wavelength of 0.086026 nm corresponding to an energy of 14.4125 keV (1 meV bandwidth). Panel (c) shows data collected at APS 13-ID-D with an X-ray wavelength of 0.0344 nm corresponding to an energy of 36.0 keV (1 eV bandwidth). The X-ray focal spots are aligned to the melted areas on the sample. (For interpretation of the references to color in this figure legend, the reader is referred to the web version of this article.)

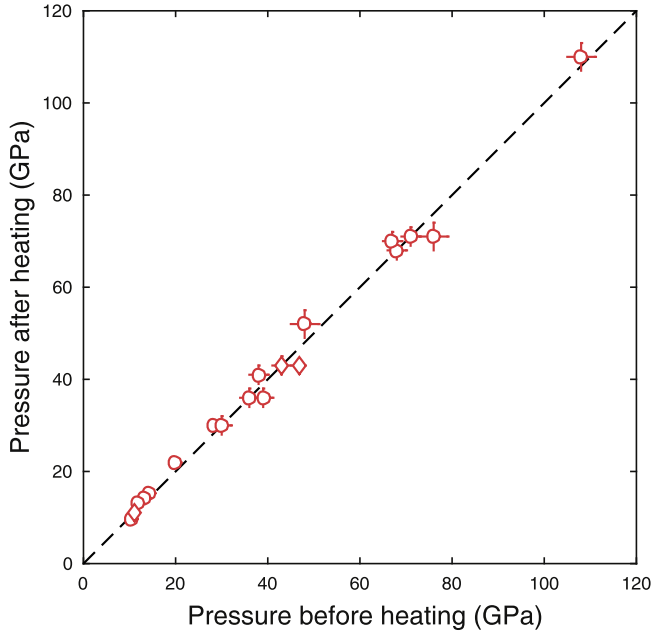

Fig. 2. Comparison of the pressure determination at 300 K using XRD of pre-melted samples (horizontal axis) and post-melted samples (vertical axis). The black dashed line is the identity line. Circles: $Fe_{0.9}Ni_{0.1}$. Diamonds: Fe. Pressures are calculated from *fcc*- and *hcp*-iron's equation of state (Dewaele et al., 2006; Komabayashi, 2014).

same beamline to determine the crystal symmetry and pressure of the sample (Figs. 1 and 2). This is achieved by moving a high resolution MAR image plate (Marresearch GmbH), located 0.3 m downstream of the DAC, into the X-ray path. Some diffraction patterns are collected at APS beamline 13-ID-D using a MARCCD detector (Rayonix) (Fig. 1c), where 36.0 keV X-rays with 1 eV bandwidth are focused to $\sim 3 \times 3\ \mu m^2$. CeO_2 and LaB_6 standards are used to calibrate the sample to image plate distance and correct for the tilt of the image plate at 3-ID-B and 13-ID-D. The diffraction images are integrated into angular resolved files using the DIOPTAS software (Prescher and Prakapenka, 2015).

After a diffraction image is collected, the image plate is moved out of the X-ray path for the series of SMS measurements that constrain the melting point. The SMS signal is captured by an avalanche photodiode detector placed ~0.5 m downstream of the sample, to avoid signal contamination by incoherently scattered photons. For each melting run, a high-statistical quality reference SMS spectrum is collected for about 10 minutes at 300 K at the sample position where the melting measurement will be carried out. The sample is then scanned in both x and y directions to record sample topography with respect to alignment of the X-ray and IR laser focal areas. Then, we heat the sample to about 1500 K, balancing the laser power upstream and downstream to achieve similar CCD readout temperatures, thus suggesting a uniformly heated sample. Another high-statistical quality SMS spectrum is collected at this elevated temperature (Fig. 3). This particular SMS spectrum provides the timing window and effective thickness of the sample at a reference elevated temperature immediately preceding the melting run, necessary components for determination of the melting point.

Before discussing the next sequence of events for melting temperature determination, we describe the profile, $S(t, \eta)$, of the time resolved delayed counts, the SMS spectrum. The SMS spectrum depends on the level splitting of the resonant nuclei, the effective thickness of the sample, η (as described above), and the time, t, relative to the excitation by the X-ray pulse. For *fcc* and *hcp* Fe and $Fe_{0.9}Ni_{0.1}$, it is known that the nuclear levels of ^{57}Fe are un-split (Macedo and Keune, 1988). Therefore S reduces to

$$S(t,\eta) = \eta^2 e^{-t/\tau} \frac{J_1^2(\sqrt{\eta t/\tau})}{\eta t/\tau} \quad , \tag{2}$$

where J_1 is the first order Bessel function of the first kind, and τ is the life time of the excited nuclear state (141 ns for ^{57}Fe) (e.g., Sturhahn, 2000; Jackson et al., 2013). The sample's effective thickness at 1500 K, which is also the initial effective thickness for the melting run, is then obtained by fitting the measured SMS spectrum to the profile given by equation (2).

Melt detection using SMS aims at determining the effective thickness as defined by equation (1) as a function of temperature. In the liquid state, the Lamb–Mössbauer factor and thus the effective thickness vanishes. In an experiment, the measurement of the time-integrated SMS signal is therefore sufficient if the nuclear level splitting is known as in our case. The measured time-integrated SMS signal is then given by

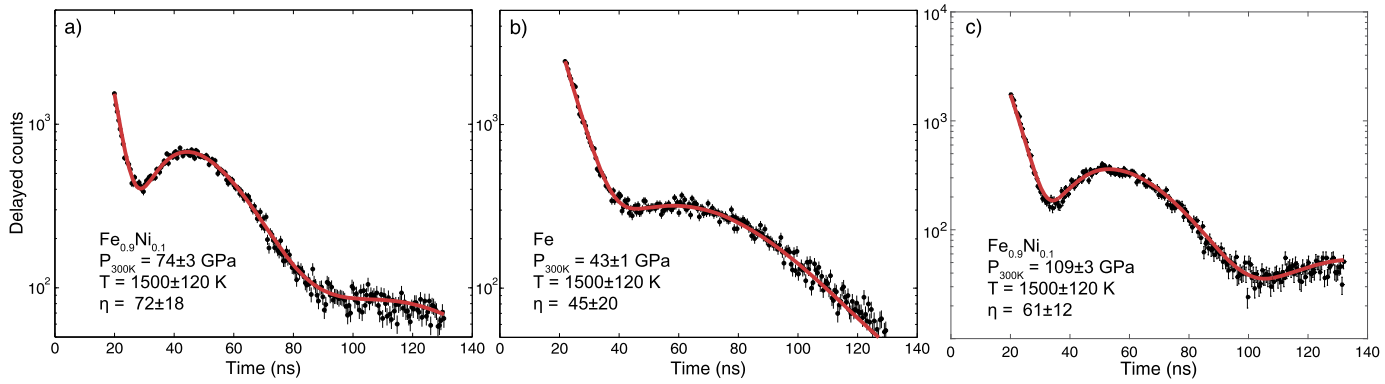

Fig. 3. SMS spectra of $^{57}Fe_{0.9}Ni_{0.1}$ and ^{57}Fe at high pressures and high temperatures. Each spectrum is collected for about 10 minutes. The SMS spectra provide the time window and are fitted to the profile given by equation (2) to determine the effective thickness. The red curves show the best-fits. The temperature shown here is determined from an average of the upstream and downstream CCD and FasTeR spectrometers over the data collection time. Pressures and their errors at 300 K are shown. (a): $^{57}Fe_{0.9}Ni_{0.1}$ at $P_{300\ K} = 74 \pm 3$ GPa and 1500 ± 120 K. The best-fit effective thickness is 72 ± 18. (b): ^{57}Fe at $P_{300\ K} = 43 \pm 1$ GPa and 1500 ± 120 K. The best-fit effective thickness is 45 ± 20. (c): $^{57}Fe_{0.9}Ni_{0.1}$ at $P_{300\ K} = 109 \pm 3$ GPa and 1500 ± 120 K. The best-fit effective thickness is 61 ± 12. (For interpretation of the references to color in this figure legend, the reader is referred to the web version of this article.)

$$I(\eta) = A\, e^{-\mu d} \sum_{n=0}^{\infty} \int_{t_1+nt_B}^{t_2+nt_B} S(t', \eta) dt' \quad . \tag{3}$$

Here t_1 and t_2 are the beginning and end of the accessible time window, t_B is the time interval between subsequent X-ray pulses (given by the synchrotron operation mode, here $t_B = 153$ ns), n is indexing X-ray pulses into the past, A is a scaling factor that depends on experimental conditions such as spectral X-ray flux incident on the sample, d is the physical thickness of the sample, μ is the electronic absorption coefficient of the sample material, S is the profile of the SMS spectrum specified in equation (2), and η is the temperature-depended effective thickness of the sample (Jackson et al., 2013).

After collecting a high temperature SMS spectrum, we immediately proceed to a computer-controlled acquisition sequence, which constitutes the melting run. In this sequence, the laser power is ramped up every 3 seconds while recording salient parameters, such as laser power, time-integrated SMS spectrum (delayed counts), X-ray intensities upstream and downstream of the sample via ionization chambers, and temperature readouts from FasTeR and the CCD spectrometer. The downstream X-ray intensity is used to normalize the time-integrated SMS spectrum which accounts for the electronic absorption term in equation (3) and for potential upstream X-ray intensity fluctuations. As described in Zhang et al. (2015), the temperature of the sample is recorded simultaneously by the FasTeR system and by upstream/downstream CCD spectrometers. Since the FasTeR system has a high sampling frequency, the FasTeR temperature is reported as the average of about 300 samplings for each 3 s interval. The temperature obtained from the CCD-based spectrometer is measured once for each 3 s interval using the SpecT code (Shen et al., 2001) and is reported as the average of upstream and downstream temperatures. The CCD-based spectrometer in this study tends to underestimate the sample temperature compared to the FasTeR measurement, because the CCD-based spectrometer has a slightly larger aperture (Zhang et al., 2015). Therefore, the temperatures determined from the FasTeR system are used in determination of the melting temperatures (Tables 1 and 2, Section 3.2). Sample temperature and normalized time-integrated delayed counts are shown as a function of laser power for three typical melting runs in Fig. 4. One can see that the duration of a melting run typically ranges from about two to four minutes.

Immediately after a melting run is completed on a localized region of the sample, the laser power is shut off, and a high statistical quality SMS spectrum is acquired. The sample is then scanned in both x and y directions to assess whether sample topography has changed with respect to scans before the melting run (i.e., to confirm that the sample area is relatively flat). Finally, we determine the sample pressure using *in situ* XRD (or *ex situ* ruby fluorescence) to document any pressure drift during the experiment. The pressure of the sample at 300 K is reported as the average of the pressures determined before and after heating. We also examine the Ni/Fe atomic ratios of the melted and unmelted regions on one $Fe_{0.9}Ni_{0.1}$ sample (recovered from D1R9, Table 1) using the EPMA facility at Caltech. The average Ni/Fe atomic ratio for the unmelted regions is $9.91 \times 10^{-2} \pm 6.5 \times 10^{-3}$ (25 data points), and the average Ni/Fe atomic ratio for the melted regions is $9.51 \times 10^{-2} \pm 1.19 \times 10^{-2}$ (18 data points). The Ni/Fe atomic ratios in the melted regions have more scatter because the melted regions have more relief at the surface. Within our experimental uncertainty, there is no clear evidence for nickel segregation in the melted regions.

3. Results and discussion

3.1. Thermal contribution to the pressure

In all of our experiments, *hcp*-structured Fe and $Fe_{0.9}Ni_{0.1}$ are observed at 300 K. The thermal equations of state from Komabayashi (2014) and Dewaele et al. (2006) are used to calculate the pressures for *fcc*- and *hcp*-phases, respectively. The pressures determined from ruby fluorescence and XRD are consistent within their relatively large error bars. Pressure uncertainties determined from the rubies are large due to their spread in values around the sample chamber and/or changes during a melting run. The quoted uncertainty for pressure determined using XRD can be large due to the limited number of accessible diffraction peaks at 14.4125 keV, despite the use of cBN backing plates. The final pressure we report is that determined from XRD (when available), measured at the same location on the sample where it is melted. In some of the melting runs, we collect a series of diffraction images, first at 300 K before heating, then at high temperatures to constrain the trend of thermal contribution to pressure, and finally at 300 K after heating, to constrain any pressure drifts (Fig. 1, Section 2.2).

In order to determine the thermal pressure contribution at the sample's melting point, we assume that: *fcc*-Fe and *fcc*-$Fe_{0.9}Ni_{0.1}$ share the same thermoelastic parameters as *hcp*-Fe and *hcp*-$Fe_{0.9}Ni_{0.1}$ and thermal pressure is only a function of temperature. The first assumption has been adopted by an XRD study using resistive heating (Komabayashi et al., 2009) and is observed in

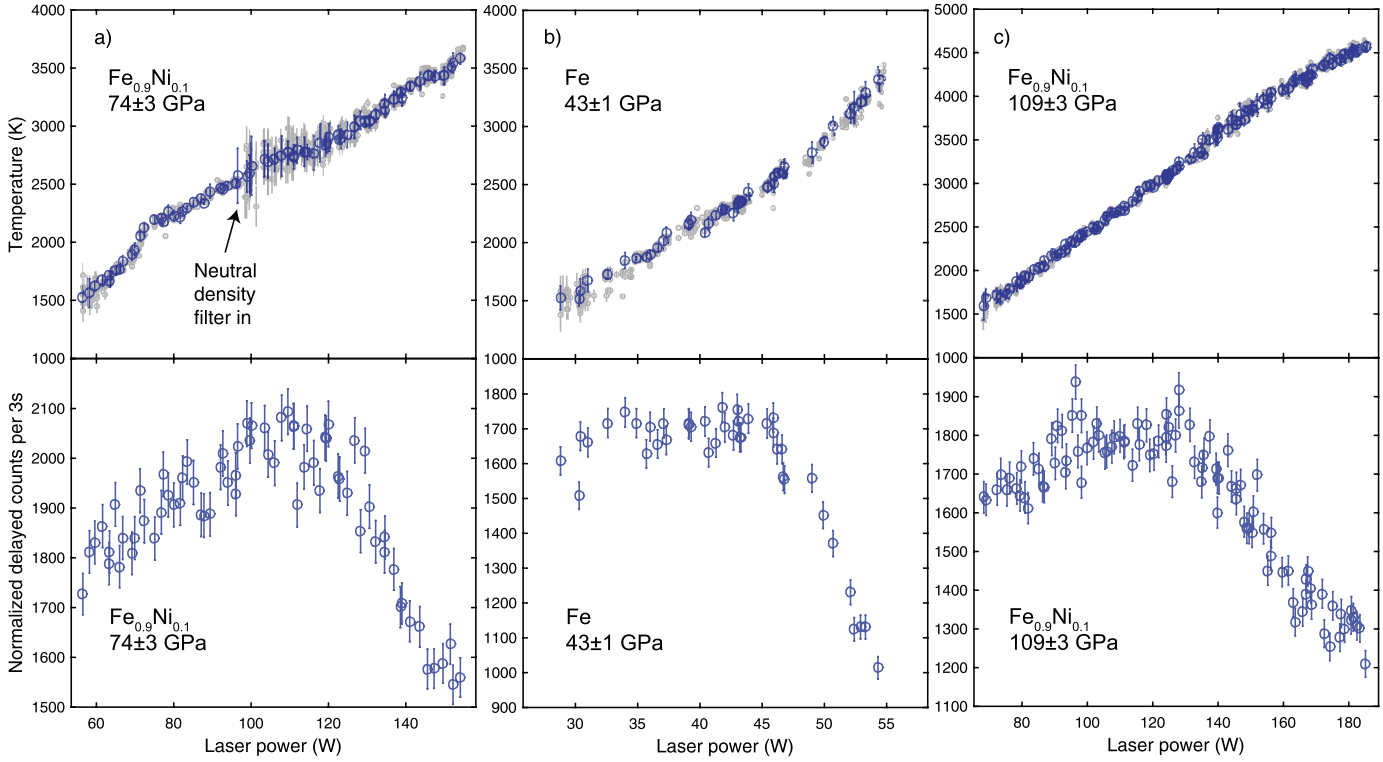

Fig. 4. Temperatures and time-integrated normalized delayed counts as a function of laser power. Sample composition, pressure and pressure error at 300 K are indicated in each panel. Temperatures are determined by the FasTeR system. Both un-binned (light grey) and binned (blue) temperatures are shown in the top panels. Binned temperatures and their standard deviations are used in determining the melting temperatures (Fig. 6). The melting run in panel (a) required insertion of a neutral density filter at ∼100 W laser power to avoid saturation. Panels (a) and (c) display data corresponding to melting runs D1R9 and D4R3 in Table 1. Panel (b) display data corresponding to melting run D6R6 in Table 2. The duration of a melting run typically ranges from about two to four minutes. (For interpretation of the references to color in this figure legend, the reader is referred to the web version of this article.)

LH-DAC XRD experiments (Anzellini et al., 2013). The addition of ∼10% Ni is suggested to have minor effect on the thermal pressure determination (Komabayashi et al., 2012). The second assumption is supported by nuclear resonant inelastic scattering experiments on *hcp*-Fe at high pressures which report a weak volume dependence of the vibrational thermal pressure up to 171 GPa (Murphy et al., 2011).

At the melting temperature T_m, the sample's pressure can be written as

$$P(T_m) = P(T_0) + P_{th}(T_m) \quad , \tag{4}$$

where $P(T_0)$ is the pressure at reference temperature $T_0 = 300$ K. The thermal pressure

$$P_{th}(T_m) = a\,(T_m - T_0) + c\,(T_m^2 - T_0^2) \tag{5}$$

has two contributions: a linear term arising from the harmonic component of the vibrational thermal pressure; a quadratic term originating from the anharmonic and electronic components (Anderson, 1980; Dewaele et al., 2006; Murphy et al., 2011). Values of $a = (4.6 \pm 0.5) \times 10^{-3}$ GPa/K and $c = (0.2 \pm 3.4) \times 10^{-6}$ GPa^2/K^2 are obtained from a best fit to data from our high P–T diffraction measurements (Figs. 1 and 5).

For reference, we also show thermal pressures determined from recent high pressure and temperature XRD studies on Fe and Fe–Ni (Komabayashi et al., 2009, 2012; Anzellini et al., 2013). A subset of the data from Komabayashi et al. (2009, 2012) and Anzellini et al. (2013) shows signs of relaxation during heating as pressure changes significantly when temperature is increased. Because Anzellini et al. (2013) didn't provide the volumes (pressures) of the Fe sample at 300 K, we cannot directly compare their thermal pressures with our results. Instead, we compare the relative pressure change between two different elevated temperatures. We assume that in each heating run from Anzellini et al. (2013) the thermal pressure of the first data point follows equation (5), and the thermal pressures of subsequent data points in the same heating run are calculated by integration of subsequent relative pres-

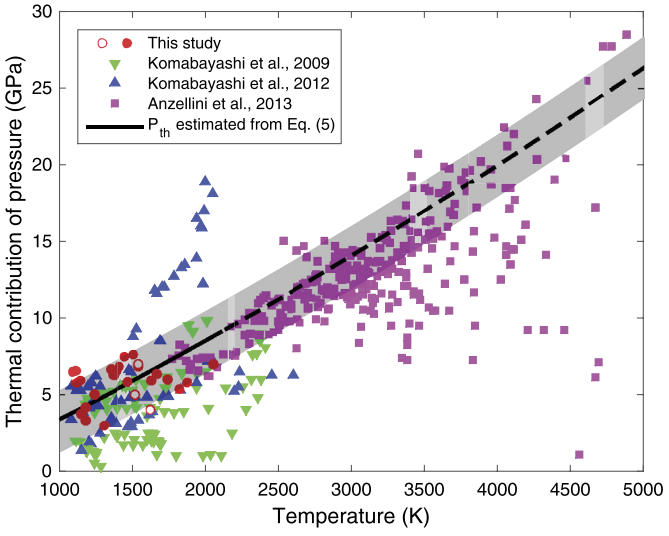

Fig. 5. Thermal pressure derived from XRD data at high pressure and temperature. Pressures of the data points at 300 K range from 10 GPa to 150 GPa. Solid circles (this study): XRD data taken at 13-ID-D. Empty circles (this study): XRD data taken at 3-ID-B. Black curve (this study): thermal contribution to pressure estimated from equation (5). Grey shaded region: estimated uncertainty of the thermal contribution to pressure. The dashed part of the curve is extrapolated. Resistive heating and optical spectroscopy temperature reading are used in Komabayashi et al. (2009, 2012). *fcc*- and *hcp*-Fe's equations of state from Komabayashi (2014) and Dewaele et al. (2006) are used to determine the pressure.

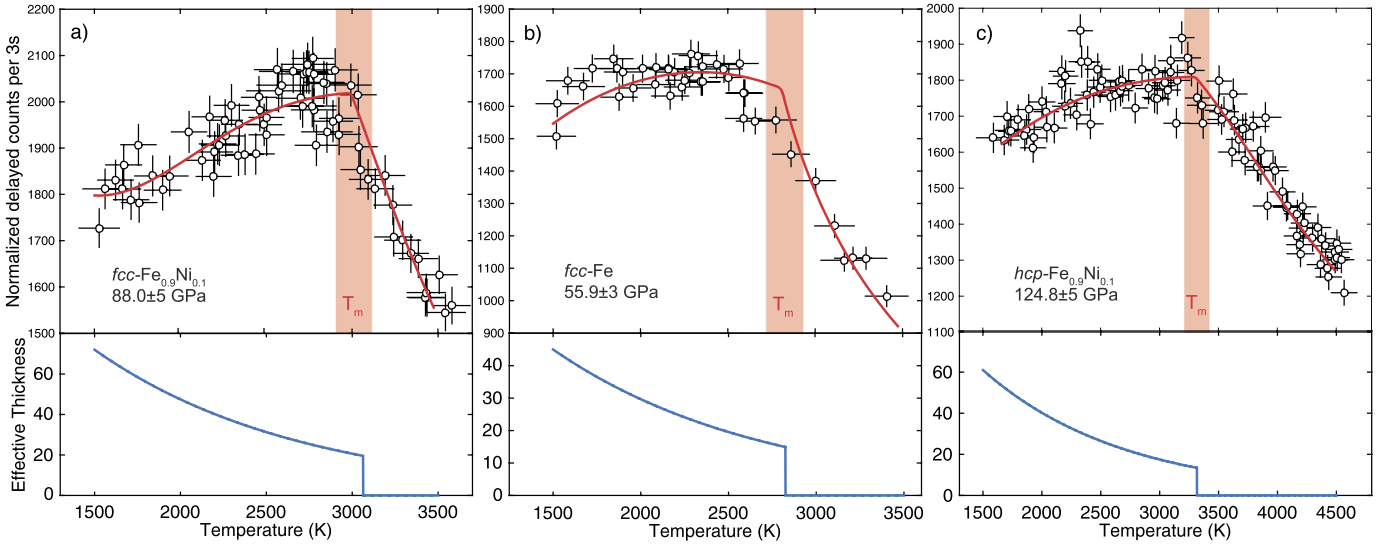

Fig. 6. Time-integrated normalized delayed counts (top panels) and calculated effective thicknesses (bottom panels) as a function of temperature for typical melting runs. Panels (a) and (c) display data corresponding to melting runs D1R9 and D4R3 in Table 1. Panel (b) displays data corresponding to melting run D6R6 in Table 2. Sample composition and pressure are indicated in each panel. Pressure values include the thermal contribution at the melting point, and temperatures are determined using the FasTeR spectrometer. The solid curves result from fits using the SIMX module of the MINUTI software package (Sturhahn, 2015). Best-fit melting temperatures and uncertainties are indicated as the red bands in the figure panel (a) $T_m = 3059 \pm 106$ K, $\chi^2 = 1.4 \pm 0.1$; panel (b) $T_m = 2835 \pm 114$ K, $\chi^2 = 1.5 \pm 0.2$; panel (c) $T_m = 3317 \pm 104$ K, $\chi^2 = 1.1 \pm 0.1$. (For interpretation of the references to color in this figure legend, the reader is referred to the web version of this article.)

sure changes. The thermal pressure trend as a function of temperature defined by equation (5) is slightly higher than that observed by Anzellini et al. (2013) (Fig. 5). In general, the thermal pressures observed in these studies are about half of the constant-volume values for *hcp*-Fe from an *ab initio* calculation (Dewaele et al., 2006) and nuclear resonant inelastic X-ray scattering measurements (Murphy et al., 2011). A similar effect was reported for laser-heated platinum in an argon medium (Goncharov et al., 2010). Based on the scatter in these independent measurements, we assess a reasonable error estimate on the thermal pressure (Tables 1 and 2).

3.2. Melting temperature determination

The melting temperatures of Fe and $Fe_{0.9}Ni_{0.1}$ are determined by fitting the measurable quantity, namely normalized delayed counts, as a function of sample temperature using the SIMX module of the MINUTI software package (Sturhahn, 2015) (Fig. 6). The effective thickness of the sample is determined immediately before the melting run begins, at around 1500 K (Fig. 3). The laser's hotspot profile is estimated from optical observation, and the X-ray focus profile is determined by knife-edge scanning. Both profiles are provided as inputs to SIMX to determine the effective thickness distribution weighted by the X-ray intensity distribution. From equations (2) and (3) and the assumption of zero effective thickness of melted material, SIMX calculates the normalized delayed intensity as a function of sample temperature and provides a fit to the measured data. For the fitting procedure, uncertainties of temperature and of the time-integrated normalized delayed counts must be provided. The latter are simply given as the square root of accumulated counts in the collection time span (3 s in our case), and the temperature uncertainties are the sum of the standard deviation of all FasTeR readings during the 3 s collection span (Fig. 4), the root-mean-square value of the dark current fluctuation, and chromatic aberration, as described in detail previously (Zhang et al., 2015). These uncertainties are displayed in Fig. 6. The fitting error of the melting point, along with its associated reduced χ^2 value from SIMX are reported in Tables 1 and 2. The uncertainty for a melting temperature is reported as the quadrature sum of the SIMX fitting error, the temperature difference of values given by the upstream and downstream CCD-based spectrometers, chromatic aberration of the CCD system (about 10 K), and the appropriate level of uncertainty assessed from the spectroradiometric method and detailed balance principle (100 K) (Sturhahn and Jackson, 2007; Zhang et al., 2015). The melting temperatures, pressures, and all associated parameters obtained in this study are summarized in Tables 1 and 2.

3.3. Melting curves of the fcc-phases and triple points

Melting temperatures and pressures obtained in this study (Tables 1 and 2) are now used to construct melting curves of *fcc*-structured Fe and $Fe_{0.9}Ni_{0.1}$ (Fig. 7). The reported pressures include the 300 K value and the high temperature contribution. The 300 K pressures are determined before and after the melting runs on annealed samples by X-ray diffraction (or ruby fluorescence) (Fig. 2), and the high temperature contributions are calculated from equation (5) as outlined in Section 3.1. At ambient pressure, a very narrow two-phase field, reported to be less than 10 K wide (Cacciamani et al., 2010), exists for *fcc*-$Fe_{0.9}Ni_{0.1}$ and liquid. However, the precision of our high-pressure measurements is not sufficient to identify such a coexistence region.

The shape of the melting curve has been modeled previously using the empirical Simon–Glatzel equation (Murphy et al., 2011; Anzellini et al., 2013)

$$T_m = T_{m0}\left(\frac{P_m - P_{m0}}{x} + 1\right)^y \quad , \tag{6}$$

where melting points (P_m, T_m) are related to a reference melting point (P_{m0}, T_{m0}), and x, y are adjustable, material specific parameters. In our study, the best-fit parameters are: $T_{m0} = 2194 \pm 100$ K, $P_{m0} = 21.4 \pm 0.9$ GPa, $x = 20 \pm 5$ GPa, and $y = 0.25 \pm 0.04$ for Fe; $T_{m0} = 2199 \pm 100$ K, $P_{m0} = 21.5 \pm 0.7$ GPa, $x = 18 \pm 3$ GPa, and $y = 0.22 \pm 0.02$ for $Fe_{0.9}Ni_{0.1}$. The corresponding melting curves are shown in Fig. 7. Considering uncertainties, these melting curves overlap in the tails of their one sigma confidence regions.

The γ–ϵ–l triple points of Fe and $Fe_{0.9}Ni_{0.1}$ are constrained by the γ–ϵ phase boundary reported in previous studies. Komabayashi et al. (2009, 2012) measured the γ–ϵ boundary of Fe and an

Table 1
Experimental results and melting points of $Fe_{0.9}Ni_{0.1}$ determined by synchrotron Mössbauer spectroscopy.

Run number	Volume[a] (cc/mol)	P_{XRD} (GPa)	P_{ruby} (GPa)	P_m (GPa)	Density[b] (g/cm^3)	Effective thickness	SIMX reduced χ^2	SIMX fitting error (K)	Time window (ns)	T_m (K)
fcc-$Fe_{0.9}Ni_{0.1}$										
D1R2	6.38 ± 0.02	10.1 ± 0.4	10 ± 1	19.0 ± 2.4	8.93 ± 0.03	89 ± 20	0.7 ± 0.3	72	10.1–124.6	2081 ± 123
D1R1	6.38 ± 0.02	10.1 ± 0.4	10 ± 1	19.2 ± 2.4	8.93 ± 0.03	124 ± 22	0.9 ± 0.2	22	10.1–124.6	2127 ± 102
D10R4	NA	NA	12.5 ± 0.8	22.2 ± 2.8	(9.0 ± 0.1)	100 ± 22	0.9 ± 0.2	26	16.1–136.0	2233 ± 103
D10R1	NA	NA	13.6 ± 0.5	23.3 ± 2.5	(9.07 ± 0.05)	43 ± 15	1.0 ± 0.3	71	18.0–137.3	2246 ± 123
D10R3	NA	NA	13.6 ± 0.5	23.3 ± 2.5	(9.07 ± 0.05)	53 ± 26	1.2 ± 0.2	29	12.3–135.2	2243 ± 104
D10R2	NA	NA	13.6 ± 0.5	23.6 ± 2.5	(9.07 ± 0.05)	70 ± 17	0.7 ± 0.2	22	12.3–135.2	2296 ± 102
D9R2	NA	NA	14.7 ± 0.6	24.7 ± 2.6	(9.12 ± 0.07)	45 ± 26	0.9 ± 0.2	48	12.5–136.2	2279 ± 111
D9R1	NA	NA	14.7 ± 0.6	24.9 ± 2.6	(9.12 ± 0.07)	73 ± 42	0.6 ± 0.2	30	11.2–136.2	2331 ± 104
D7R2	NA	NA	21.3 ± 1	32.0 ± 3	(9.4 ± 0.1)	35 ± 15	1.1 ± 0.4	100	18.9–135.7	2411 ± 141
D7R3	NA	NA	21.3 ± 1	32.0 ± 3	(9.4 ± 0.1)	55 ± 25	0.8 ± 0.4	38	19.0–136.1	2410 ± 107
D7R1	NA	NA	21.3 ± 1	32.1 ± 3	(9.4 ± 0.1)	31 ± 11	1.9 ± 0.6	130	19.6–135.7	2423 ± 164
D9R5	NA	NA	29.3 ± 1	40.7 ± 3	(9.6 ± 0.1)	61 ± 9	1.5 ± 0.3	84	15.8–135.9	2530 ± 131
D9R3	NA	NA	29.3 ± 1	40.9 ± 3	(9.6 ± 0.1)	63 ± 15	0.8 ± 0.1	21	15.9–136.5	2574 ± 103
D9R4	NA	NA	29.3 ± 1	41.0 ± 3	(9.6 ± 0.1)	70 ± 14	1.1 ± 0.2	62	16.1–135.4	2602 ± 112
D1R5	5.95 ± 0.05	30.0 ± 1	30.0 ± 3	41.8 ± 3	9.6 ± 0.1	106 ± 35	2.1 ± 0.3	57	18.2–139.5	2645 ± 115
D1R3	5.92 ± 0.04	36.0 ± 1	38.0 ± 2	47.8 ± 3	9.8 ± 0.1	16 ± 9	1.1 ± 0.3	130	15.8–135.8	2619 ± 164
D1R4	5.92 ± 0.04	36.0 ± 1	38.0 ± 2	48.3 ± 3	9.8 ± 0.1	16 ± 9	2.9 ± 0.4	130	15.8–135.8	2715 ± 164
D3R1	5.76 ± 0.04	37.5 ± 1	39.0 ± 3	49.8 ± 3	9.9 ± 0.1	43 ± 20	1.1 ± 0.3	48	19.3–132.7	2716 ± 111
D8R1	5.76 ± 0.04	39.0 ± 1	37.5 ± 2	50.7 ± 3	9.9 ± 0.1	68 ± 18	1.3 ± 0.2	21	16.4–139.5	2598 ± 102
D8R2	5.76 ± 0.04	39.0 ± 1	37.5 ± 2	51.1 ± 3	9.9 ± 0.1	45 ± 26	1.0 ± 0.2	14	18.0–139.5	2683 ± 101
D1R6	5.62 ± 0.06	50.0 ± 2	52.0 ± 3	63.2 ± 4	10.2 ± 0.2	102 ± 19	1.4 ± 0.2	55	16.1–132.6	2882 ± 114
D8R5	5.44 ± 0.05	61.0 ± 1	63.0 ± 3	74.9 ± 3	10.5 ± 0.1	76 ± 13	1.3 ± 0.2	55	16.1–133.4	2966 ± 114
D1R10	5.38 ± 0.04	66.0 ± 2	66.8 ± 3	79.8 ± 4	10.6 ± 0.1	64 ± 30	1.4 ± 0.2	44	15.9–130.5	2974 ± 109
D1R11	5.38 ± 0.04	66.0 ± 2	66.8 ± 3	80.0 ± 4	10.6 ± 0.1	74 ± 14	1.2 ± 0.1	19	16.0–131.5	3017 ± 102
D8R3	5.37 ± 0.05	69.0 ± 2	63.0 ± 3	83.1 ± 4	10.7 ± 0.1	82 ± 14	0.7 ± 0.2	22	16.0–135.6	3023 ± 102
D8R4	5.37 ± 0.05	69.0 ± 2	63.0 ± 3	83.3 ± 4	10.7 ± 0.1	72 ± 13	1.2 ± 0.2	21	16.0–135.9	3056 ± 102
D4R1	5.34 ± 0.03	71.0 ± 2	71.0 ± 2	85.1 ± 4	10.7 ± 0.1	90 ± 24	4.9 ± 0.4	130	17.9–132.8	3028 ± 164
D1R9	5.28 ± 0.04	74.0 ± 3	74.3 ± 2	88.0 ± 5	10.8 ± 0.2	72 ± 15	1.4 ± 0.1	36	15.9–136.3	3059 ± 106
D1R8	5.28 ± 0.04	74.0 ± 3	74.3 ± 2	88.2 ± 5	10.8 ± 0.2	109 ± 18	1.6 ± 0.2	66	16.0–136.3	3061 ± 114
D1R7	5.28 ± 0.04	74.0 ± 3	74.3 ± 2	88.5 ± 5	10.8 ± 0.2	104 ± 18	1.2 ± 0.1	38	15.7–136.1	3103 ± 107
hcp-$Fe_{0.9}Ni_{0.1}$										
D4R3	4.96 ± 0.04	109.0 ± 3	112.0 ± 5	124.8 ± 5	11.5 ± 0.1	61 ± 12	1.1 ± 0.1	27	19.6–132.5	3317 ± 104
D4R2	4.96 ± 0.04	109.0 ± 3	112.0 ± 5	125.0 ± 5	11.5 ± 0.1	64 ± 13	1.1 ± 0.1	19	19.6–132.4	3383 ± 102
quasi γ–ϵ–*l triple point*			P: 116 ± 5 GPa				T: 3260 ± 120 K			

DXRY = DAC X Run Y.
[a] In some melting runs the limited angular access of backing plates prevented diffraction peaks to be observed (NA: not applicable), therefore pressures are determined from fluorescence of ruby spheres.
[b] Values in parentheses are calculated from pressure via the *fcc*-Fe (Komabayashi, 2014) or *hcp*-Fe (Dewaele et al., 2006) equations of state. P_m is determined by adding the thermal contribution (Eq. (5)) at the melting temperature to the pressure at 300 K.

Table 2
Experimental results and melting points of Fe determined by synchrotron Mössbauer spectroscopy.

fcc-Fe										
Run number	Volume[a] (cc/mol)	P_{XRD} (GPa)	P_{ruby} (GPa)	P_m (GPa)	Density[b] (g/cm^3)	Effective thickness	SIMX reduced χ^2	SIMX fitting error (K)	Time window (ns)	T_m (K)
D10R5	6.42 ± 0.04	10.0 ± 0.5	11.1 ± 1	19.0 ± 2.5	8.88 ± 0.05	49 ± 12	1.7 ± 0.4	25	15.8–135.7	2116 ± 103
D10R6	6.42 ± 0.04	10.0 ± 0.5	11.1 ± 1	19.1 ± 2.5	8.88 ± 0.05	53 ± 12	2.2 ± 0.4	43	15.8–135.8	2123 ± 119
D6R1	NA	NA	28.0 ± 1	39.8 ± 3	(9.6 ± 0.1)	27 ± 11	0.9 ± 0.2	190	17.8–136.4	2614 ± 215
D6R2	NA	NA	28.0 ± 1	39.8 ± 3	(9.6 ± 0.1)	28 ± 10	0.6 ± 0.2	150	18.0–135.6	2614 ± 180
D6R3	NA	NA	28.0 ± 1	40.0 ± 3	(9.6 ± 0.1)	18 ± 11	1.4 ± 0.3	230	17.8–135.7	2650 ± 251
D6R6	5.70 ± 0.03	43.0 ± 1	42.3 ± 2	55.9 ± 3	10.0 ± 0.1	49 ± 14	1.5 ± 0.2	54	21.1–136.3	2835 ± 114
D6R5	5.69 ± 0.03	44.0 ± 2	42.3 ± 2	57.1 ± 4	10.0 ± 0.2	47 ± 15	0.9 ± 0.2	29	21.0–136.5	2858 ± 104
D6R4	5.65 ± 0.03	47.0 ± 1	42.3 ± 2	59.8 ± 3	10.1 ± 0.1	53 ± 14	0.5 ± 0.1	45	21.2–135.6	2792 ± 110
γ–ϵ–*l triple point*			P: 110 ± 5 GPa				T: 3345 ± 120 K			

DXRY = DAC X Run Y.
[a] In some melting runs the limited angular access of backing plates prevented diffraction peaks to be observed (NA: not applicable), therefore pressures are determined from fluorescence of ruby spheres.
[b] Values in parentheses are calculated from pressure via the *fcc*-Fe (Komabayashi, 2014) or *hcp*-Fe (Dewaele et al., 2006) equations of state. P_m is determined by adding the thermal contribution (Eq. (5)) at the melting temperature to the pressure at 300 K.

Fe-9.7 wt% Ni alloy using resistively-heated DACs and X-ray diffraction. They reported the slope of the phase boundary dP/dT as 0.0394 GPa/K (at 88 GPa, 2800 K) for Fe and as 0.0426 GPa/K (at 61.8 GPa, 1992 K) for Fe-9.7 wt% Ni alloy, respectively. In principle, a γ–ϵ–l triple point is not meaningful for an alloy such as $Fe_{0.9}Ni_{0.1}$, because melting should be described by a solidus and liquidus. Within our experimental resolution however, the solidus and liquidus of $Fe_{0.9}Ni_{0.1}$ coincide and are addressed as the melting curve of $Fe_{0.9}Ni_{0.1}$. Accordingly we define a quasi γ–ϵ–l triple point for $Fe_{0.9}Ni_{0.1}$ as the intersection of γ–ϵ phase boundary and melting curve. By combining the *fcc*–*hcp* boundaries from Komabayashi et al. (2009, 2012) and our *fcc* melting curves, the γ–ϵ–l triple points of Fe and $Fe_{0.9}Ni_{0.1}$ are calculated to be 110 ± 5 GPa, 3345 ± 120 K and 116 ± 5 GPa, 3260 ± 120 K, respec-

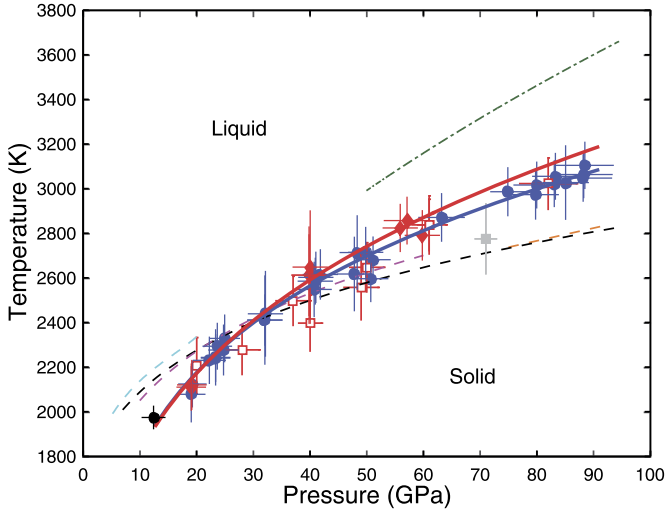

Fig. 7. Melting points of *fcc*-structured Fe and $Fe_{0.9}Ni_{0.1}$. Solid blue circles and red diamonds (this study): $Fe_{0.9}Ni_{0.1}$ and Fe. Blue and red solid curves (this study): best-fits for $Fe_{0.9}Ni_{0.1}$ and Fe using equation (6). The following studies include thermal contributions: empty squares (Jackson et al., 2013), dark green dash-dotted curve (Anzellini et al., 2013), orange dashed curve (Aquilanti et al., 2015), grey square: shock compression (Ahrens et al., 2002). Black solid circle: Strong et al. (1973), corrected with thermal contribution of pressure using Eq. (5). The following studies did not consider thermal pressure: black dashed curve (Boehler et al., 1990; Boehler, 1993), magenta dashed curve (Shen et al., 1998, 2004), cyan dashed curve (Liu and Bassett, 1975). All experiments except for Ahrens et al. (2002) were carried out with laser-heated diamond anvil cells. (For interpretation of the references to color in this figure legend, the reader is referred to the web version of this article.)

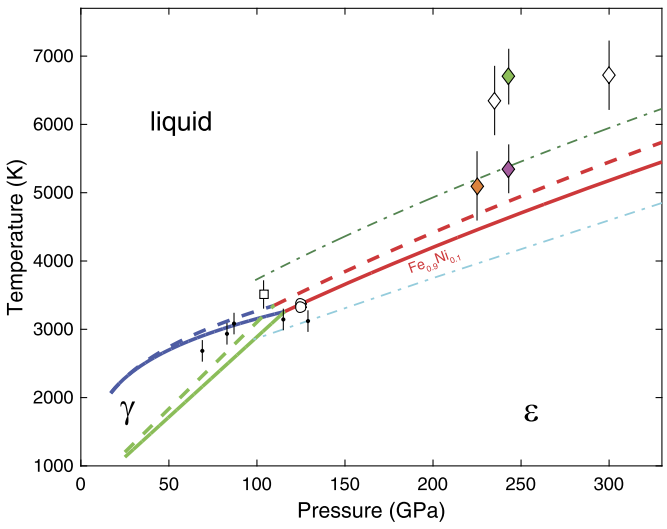

Fig. 8. Phase boundaries of Fe and $Fe_{0.9}Ni_{0.1}$. Dashed curves and solid curves are for Fe and $Fe_{0.9}Ni_{0.1}$, respectively (this study), where the γ–ϵ boundaries of Fe and $Fe_{0.9}Ni_{0.1}$ are adapted from Komabayashi et al. (2009, 2012). The empty circles are for *hcp*-$Fe_{0.9}Ni_{0.1}$ (this study, error bars are smaller than the symbols). Dash-dotted curves: Fe ϵ–l boundary (dark green: Anzellini et al., 2013, cyan: Boehler, 1993). Black dots: Fe solid-liquid boundary (Boehler et al., 2008). Empty square: *hcp*-Fe in LH-DAC, XRD (Ma et al., 2004). Diamonds: *hcp*-Fe, shock compression experiments (orange: Nguyen and Holmes, 2004, magenta: Brown and McQueen, 1986, green: Bass et al., 1987, empty: Yoo et al., 1993). (For interpretation of the references to color in this figure legend, the reader is referred to the web version of this article.)

tively (Fig. 8). The triple point of Fe is found at higher temperature and lower pressure than the quasi triple point of $Fe_{0.9}Ni_{0.1}$, a trend suggested by ambient pressure experiments (see Cacciamani et al., 2010 and references therein).

3.4. Melting curves of the hcp-phases

Two melting experiments are carried out for $Fe_{0.9}Ni_{0.1}$ at pressures above 100 GPa. The pressure of the $Fe_{0.9}Ni_{0.1}$ sample at room temperature is 109 ± 3 GPa, determined by XRD (Table 1). The same sample is melted twice at two locations, spatially separated by ~20 μm. The best-fit melting temperatures of the two runs are 3383 ± 102 K and 3317 ± 104 K as determined by SIMX. The thermal contribution according to equation (5) is included to provide pressures at melting as 125 ± 5 GPa and 124.8 ± 5 GPa, respectively (Fig. 8). These melting points are at higher pressures and temperatures than the quasi γ–ϵ–l triple point, and we can infer that melting of the *hcp*-phase of $Fe_{0.9}Ni_{0.1}$ was observed in these two melting runs. In order to extrapolate the high pressure melting curves of *hcp*-structured Fe and $Fe_{0.9}Ni_{0.1}$ to inner core conditions, we apply the Simon–Glatzel equation (6) and the (quasi) triple points determined earlier as anchor points, T_{m0} and P_{m0}. The other two parameters in the Simon–Glatzel equation are obtained from the phonon density-of-states of *hcp*-Fe measured by nuclear resonant inelastic X-ray scattering by a procedure outlined in Section 4 of Murphy et al. (2011). This method makes the reasonable assumption that the vibrational behavior of *hcp*-structured Fe and $Fe_{0.9}Ni_{0.1}$ are very similar. Then the best-fit parameters in the Simon–Glatzel equation are: $x = 171 \pm 20$ GPa, $y = 0.63 \pm 0.08$ for *hcp*-$Fe_{0.9}Ni_{0.1}$, and $x = 167 \pm 20$ GPa, $y = 0.64 \pm 0.08$ for *hcp*-Fe. These melting curves, which are shown in Fig. 8, predict for *hcp*-$Fe_{0.9}Ni_{0.1}$ a melting temperature of 3370 ± 120 K at 125 GPa, demonstrating consistency with the measured values of 3383 ± 102 K and 3317 ± 104 K.

Melting curves of Fe–Ni alloys at high pressures were not reported previously, but a comparison of the obtained melting curves for Fe with previous studies is possible. A wide range of criteria were used in those studies to determine melting: Liu and Bassett (1975) and Boehler et al. (1990) measured the resistivity of Fe at different temperatures; Williams et al. (1987), Boehler et al. (1990), and Boehler (1993) monitored the surface properties of Fe, such as optical reflectivity, texture and convective motion; diffuse scattering observed in an XRD setup has been used recently (Shen et al., 1998, 2004; Anzellini et al., 2013); X-ray absorption spectroscopy has also been used to monitor phase transitions of Fe (Aquilanti et al., 2015).

These methods have different sensitivities to the onset of melting. Monitoring the surface properties is not sensitive to the interior of the sample and can be dependent on sample-specific surface and interface properties. X-ray based methods, such as monitoring diffuse scattering (X-ray diffraction), short-range coordination environment (X-ray absorption), and atomic dynamics (synchrotron Mössbauer spectroscopy), are more sensitive to the entire scattering volume of the sample. Thermal diffuse scattering is sensitive to the average electronic arrangement of the material during the X-ray diffraction exposure time (Shen et al., 2004; Dewaele et al., 2007, 2010; Anzellini et al., 2013). The presence of melt is identified by the appearance of broad diffuse rings in the X-ray diffraction pattern characterizing the disappearance of long range coordination environments in the melt. The thermal diffuse scattering signal must be discriminated against a relatively large background signal and likely requires a large volume of melt in the scattering volume. X-ray absorption spectroscopy monitors the average short-range coordination of the absorbing atoms rendering a subtle change upon melting.

Synchrotron Mössbauer spectroscopy is sensitive only to the resonant nuclei in the sample and is a background free diagnostic method when used in combination with time discrimination techniques. The intensity of the time-integrated signal from synchrotron Mössbauer spectroscopy reflects the microscopic range of movement of the iron nuclei. As the solid sample transitions to a

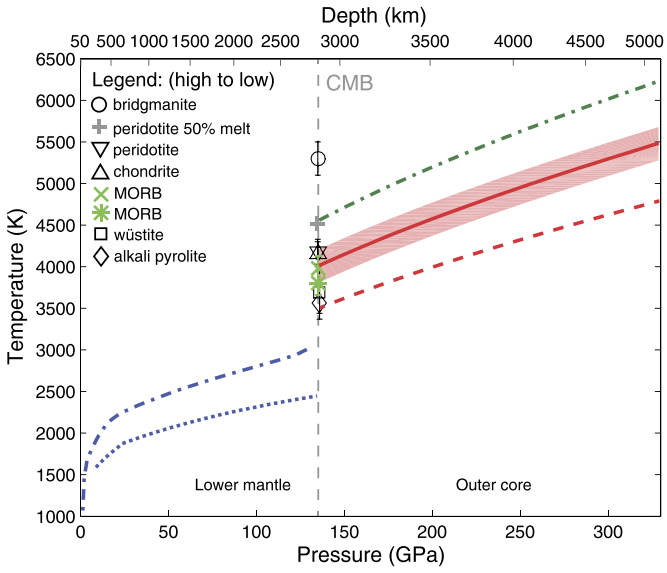

Fig. 9. Proposed thermal profiles of Earth's interior and melting points of minerals. Blue curves: proposed geotherms (dotted: Brown and Shankland, 1981; dashed: Stacey, 1977). Red solid curve: outer core temperature profile calculated from inferred melting temperature of *hcp*-$Fe_{0.9}Ni_{0.1}$ at 330 GPa, this study, red shaded region gives error estimate. Red dashed curve: outer core temperature profile calculated from our study and accounting a 700 K melting point depression at the ICB from light elements (Alfè et al., 2002). Dark green dash-dotted curve: outer core temperature profile calculated from inferred melting temperature of *hcp*-Fe at 330 GPa (Anzellini et al., 2013). Circle: bridgmanite melting point (Akins et al., 2004). Gray cross: peridotite containing about 50% melt (Tateno et al., 2014). Reversed triangle: peridotite solidus (Fiquet et al., 2010). Triangle: chondrite solidus (Andrault et al., 2011). Green cross: MORB solidus (Pradhan et al., 2015), extrapolated value from data between 44 and 128 GPa. Green asterisk: MORB solidus (Andrault et al., 2014). Square: wüstite melting point (Fischer and Campbell, 2010), extrapolated value from data between 0 and 77 GPa. Diamond: alkali pyrolite solidus (Nomura et al., 2014). The depth scale is taken from the Preliminary Reference Earth Model (Dziewonski and Anderson, 1981). (For interpretation of the references to color in this figure legend, the reader is referred to the web version of this article.)

liquid state, atoms experience an enhanced freedom of motion. For the iron nuclei this results in the absence of recoil-free scattering events. The Mössbauer signal, which is a consequence of recoil-free scattering, consequently disappears in the liquid state and drops markedly in a solid–liquid mixture (Singwi and Sjölander, 1960; Boyle et al., 1961; Jackson et al., 2013; Zhang et al., 2015). These significant differences in criteria may explain the higher melting temperatures reported for Fe using thermal diffuse scattering (Figs. 7, 8), as they are likely to represent upper bounds. The marked drop in the Mössbauer signal reliably captures the first melt to form in the sampled volume. In combination with well-calibrated temperature data from the FasTeR instrument, high-quality melting temperatures for Fe and $Fe_{0.9}Ni_{0.1}$ are obtained.

3.5. Implications for the temperature in Earth's core

The high pressure melting curves of *fcc* and *hcp* structured Fe and $Fe_{0.9}Ni_{0.1}$ constrained in this study allow one to predict the temperature in Earth's core. It is commonly assumed that addition of light elements to Fe depresses the melting point of iron alloys (Alfè et al., 2002). Therefore the melting temperatures of *hcp*-Fe and *hcp*-$Fe_{0.9}Ni_{0.1}$ at 330 GPa serve as an upper bound for the temperature at Earth's inner core–outer core boundary (T_{ICB}) (Lehmann, 1936; Terasaki et al., 2011). An extrapolation of our melting curves for *hcp*-Fe and *hcp*-$Fe_{0.9}Ni_{0.1}$ predicts upper bounds for T_{ICB} of 5700 ± 200 K and 5500 ± 200 K, respectively (Fig. 8). In this study, we assume that *hcp*-$Fe_{0.9}Ni_{0.1}$ is a more likely base composition for the core than pure *hcp*-Fe, and consequently we proceed with *hcp*-$Fe_{0.9}Ni_{0.1}$'s melting curve to constrain the upper bound of T_{ICB}.

The thermal profile in the core is commonly derived from an adiabatic model, for which the temperature gradient in the outer core is given by (Poirier, 2000)

$$\frac{\partial T}{\partial z} = \frac{g\gamma_{th}}{\Phi} T \quad , \tag{7}$$

where T is temperature, z is depth, g is gravitational acceleration, γ_{th} is the thermodynamic Grüneisen parameter, and Φ is the seismic parameter. We use the gravitational acceleration data from the PREM model (Dziewonski and Anderson, 1981) and the seismic parameter from the AK135 global seismic model (Kennett et al., 1995). For compressed liquid iron, γ_{th} was reported as ranging between 1.56 at 257 GPa and 1.47 at the ICB from shock-compression experiments (Brown and McQueen, 1986) and calculated as ranging between 1.5 and 1.53 in the outer core (Alfè et al., 2002). After combining these results into an average, we use $\gamma_{th} = 1.51$ and, with *hcp*-$Fe_{0.9}Ni_{0.1}$'s melting point of 5500 ± 200 K at the ICB, we obtain a temperature of 4000 ± 200 K at the core side of the CMB at z = 2891 km, $P = 136$ GPa (Fig. 9).

The temperature of 4000 ± 200 K that we obtain for the core side of the CMB is slightly lower than the solidus temperature of peridotitic (4180 ± 150 K, Fiquet et al., 2010) and chondritic lower mantle assemblages (4150 ± 150 K, Andrault et al., 2011) at 135 GPa (albeit in the mutual uncertainties). The extrapolated melting point of wüstite at $P = 136$ GPa is 3690 K (Fischer and Campbell, 2010). A very low solidus temperature of an alkali-rich pyrolitic sample was reported to be 3570 ± 200 K at the CMB (Nomura et al., 2014). The alkalic pyrolite starting material contains a significant amount of volatile elements (400 ppm water, ~0.4 wt% Na_2O and ~0.05 wt% K_2O) not present in other experiments (Fiquet et al., 2010; Andrault et al., 2011), and volatile elements are known to depress the solidus temperatures of mantle assemblages (Hirschmann et al., 1998; Corgne et al., 2003; Andrault et al., 2011).

We conduct similar calculations with the melting curve of *hcp*-Fe reported by Anzellini et al. (2013). Their melting temperature at 330 GPa is 6230 ± 500 K, which corresponds to a temperature of 4560 K at the core–mantle boundary using the adiabat described above. This temperature is much higher than the solidus of peridotitic (Fiquet et al., 2010; Nomura et al., 2014) and chondritic (Andrault et al., 2011) phase assemblages at the CMB, suggesting that roughly half of the base of the mantle should be molten (Tateno et al., 2014) (Fig. 9).

Although the Earth's core is mainly composed of an iron–nickel alloy, the seismologically inferred density requires the presence of light elements to balance the density deficit. Therefore, the lower bound on the temperature profile in the core depends on the species of light elements and how these elements affect the melting behavior of iron and iron–nickel alloys. Experimental and theoretical investigations suggest that light elements such as S, O, and Si alloyed with iron could depress the melting point of iron by up to 700 K at the ICB (e.g., Alfè et al., 2002). If one considers a relatively extreme melting point depression of 700 K on the temperature at the ICB inferred from *hcp*-$Fe_{0.9}Ni_{0.1}$'s melting point of 5500 K (this study), then the temperature at the ICB would be 4800 K. If the adiabat is unchanged with the addition of light elements, then the core-side CMB temperature could be as low as 3500 K (Fig. 9). Terasaki et al. (2011) measured the phase relations of a candidate core-alloy of atomic composition $Fe_{75}O_5S_{20}$ up to 157 GPa and concluded that, assuming its existence in Earth's core and comparing to previous studies on pure iron, the CMB temperature could be 3600 ± 200 K. We have observed that alloying about 10 wt% nickel to iron could result in a melting point depression relative to pure iron of about 200 K or about 4% at the ICB. Thus

it is conceivable that the melting temperatures of light element alloys of *hcp*-$Fe_{0.9}Ni_{0.1}$ would be further depressed than the values considered in Terasaki et al. (2011).

One major implication of the temperature constraints considered here is the effect on phase relations at the base of the mantle. Fits to seismic waves that sample the base of the mantle suggest ultra-low velocity zones ranging from 10's to 100 km in width and height (Berryman, 2000; Ni and Helmberger, 2001; Lay et al., 2004; McNamara et al., 2010; Sun et al., 2013; Thorne et al., 2013). These features are often attributed to partial melt of lower mantle materials (Williams and Garnero, 1996; Berryman, 2000; Lay et al., 2004; Labrosse et al., 2007; Hier-Majumder, 2008). A recent dynamic compression study suggests that a peridotitic lowermost mantle rock is unlikely to produce an equilibrium partial melt that is sufficiently dense to match seismic inferences of about +5 to 14% density anomalies (Thomas and Asimow, 2013). A similarly compelling explanation of seismic observations is solid material with low seismic velocities, such as Fe-rich (Mg,Fe)O magnesiowüstite (Wicks et al., 2010; Bower et al., 2011; Sun et al., 2013; Rost, 2013). These hypotheses can be assessed by examination of the solidus temperatures reported for candidate mantle phases and assemblages at the CMB in comparison with the temperature ranges reported for this region. The presence of partial melts at the base of the mantle is feasible if a sufficient amount of volatile elements would depress the solidus of silicate phase assemblages, so that the geotherm of the lowermost mantle intersects the solidus at just the right value and angle to generate a reasonable amount of melt.

4. Conclusion

The melting points of *fcc*- and *hcp*-structured $Fe_{0.9}Ni_{0.1}$ and Fe have been measured up to 125 GPa. We carried out these measurements with LH-DACs using newly developed techniques involving synchrotron Mössbauer spectroscopy, the FasTeR spectrometer, and the MINUTI software package. The SIMX module in MINUTI is used to reliably fit a melting point to the observed signal. We place the γ–ϵ–l triple point of Fe at 110 ± 5 GPa and 3345 ± 120 K, and the quasi triple point of $Fe_{0.9}Ni_{0.1}$ at 116 ± 5 GPa and 3260 ± 120 K. With the (quasi) γ–ϵ–l triple points and the thermophysical parameters of *hcp*-Fe determined from a nuclear resonant inelastic X-ray scattering dataset, we constructed high pressure melting curves of *hcp*-structured Fe and $Fe_{0.9}Ni_{0.1}$. We suggest that the upper bound of Earth's innercore–outercore boundary temperature is given by *hcp*-$Fe_{0.9}Ni_{0.1}$'s melting point, rather than by pure iron. With an ICB temperature of 5500 ± 200 K for *hcp*-$Fe_{0.9}Ni_{0.1}$, we use an adiabatic thermal model to derive the upper bound for the temperature on the core side of the CMB as 4000 ± 200 K. This temperature is lower than the solidus of typical lower mantle assemblages. With the addition of light elements such as a combination of sulfur, oxygen, and silicon, the core-side CMB temperature could be as low as 3500 K. These newly constrained temperature bounds will help determine the range of permissible phase assemblages and transport at the core–mantle and inner core–outer core boundaries.

Acknowledgements

We thank G. Shen, M. Rivers, Y. Meng, W. Bi, A. Alatas, B. Chen and C. Ma for useful discussions and help in conducting experiments. We thank NSF (EAR-1316362) for financial support of this research as well as GeoSoilEnviroCARS and HP-CAT for allowing access to their laser drilling and the ruby fluorescence systems. Use of GeoSoilEnviroCARS is supported by the National Science Foundation – Earth Sciences (EAR-1128799) and Department of Energy–GeoSciences (DE-FG02-94ER14466). Use of the Advanced Photon Source is supported by the U.S. D.O.E., O.S., O.B.E.S. (DE-AC02-06CH11357). Sector 3 operations are supported in part by COMPRES under NSF Cooperative Agreement EAR 06-49658. Microprobe analyses were carried out at the Caltech GPS Division Analytical Facility (funded in part by the MRSEC Program of the NSF under DMR-0080065). We would like to thank Dr. Oliver Lord and two anonymous reviewers for constructive comments, and Dr. John Brodholt for handling the manuscript.

References

Ahrens, T.J., Holland, K.G., Chen, G.Q., 2002. Phase diagram of iron, revised-core temperatures. Geophys. Res. Lett. 29 (7), 1150.

Akins, J.A., Luo, S.-N., Asimow, P.D., Ahrens, T.J., 2004. Shock-induced melting of $MgSiO_3$ perovskite and implications for melts in Earth's lowermost mantle. Geophys. Res. Lett. 31 (14), L14612. http://dx.doi.org/10.1029/2004GL020237.

Alfè, D., Gillan, M., Price, G., 2002. Composition and temperature of the Earth's core constrained by combining ab initio calculations and seismic data. Earth Planet. Sci. Lett. 195 (1–2), 91–98. http://www.sciencedirect.com/science/article/pii/S0012821X01005684.

Anderson, O.L., 1980. An experimental high-temperature thermal equation of state bypassing the Grüneisen parameter. Phys. Earth Planet. Inter. 22 (3–4), 165–172.

Anderson, O.L., 1990. The high-pressure triple points of iron and their effects on the heat flow from the Earth's core. J. Geophys. Res., Solid Earth 95 (B13), 21697–21707. http://dx.doi.org/10.1029/JB095iB13p21697.

Andrault, D., Bolfan-Casanova, N., Nigro, G.L., Bouhifd, M.A., Garbarino, G., Mezouar, M., 2011. Solidus and liquidus profiles of chondritic mantle: implication for melting of the Earth across its history. Earth Planet. Sci. Lett. 304 (1–2), 251–259. http://www.sciencedirect.com/science/article/pii/S0012821X1100077X.

Andrault, D., Bolfan-Casanova, N., Ohtaka, O., Fukui, H., Arima, H., Fialin, M., Funakoshi, K., 2009. Melting diagrams of Fe-rich alloys determined from synchrotron in situ measurements in the 15–23 GPa pressure range. Phys. Earth Planet. Inter. 174 (1–4), 181–191.

Andrault, D., Pesce, G., Bouhifd, M.A., Bolfan-Casanova, N., Hénot, J.-M., Mezouar, M., 2014. Melting of subducted basalt at the core–mantle boundary. Science 344 (6186), 892–895. http://www.sciencemag.org/content/344/6186/892.abstract.

Anzellini, S., Dewaele, A., Mezouar, M., Loubeyre, P., Morard, G., 2013. Melting of iron at Earth's inner core boundary based on fast X-ray diffraction. Science 340 (6131), 464–466.

Aquilanti, G., Trapananti, A., Karandikar, A., Kantor, I., Marini, C., Mathon, O., Pascarelli, S., Boehler, R., 2015. Melting of iron determined by x-ray absorption spectroscopy to 100 GPa. Proc. Natl. Acad. Sci. 112 (39), 12042–12045. http://www.pnas.org/content/112/39/12042.abstract.

Asanuma, H., Ohtani, E., Sakai, T., Terasaki, H., Kamada, S., Kondo, T., Kikegawa, T., 2010. Melting of iron–silicon alloy up to the core–mantle boundary pressure: implications to the thermal structure of the Earth's core. Phys. Chem. Miner. 37 (6), 353–359.

Bass, J.D., Svendsen, B., Ahrens, T.J., 1987. The temperature of shock compressed iron. In: High-Pressure Research in Mineral Physics: A Volume in Honor of Syun-iti Akimoto, pp. 393–402.

Berryman, J.G., 2000. Seismic velocity decrement ratios for regions of partial melt in the lower mantle. Geophys. Res. Lett. 27 (3), 421–424. http://dx.doi.org/10.1029/1999GL008402.

Boehler, R., 1992. Melting of the Fe–FeO and the Fe–FeS systems at high pressure: constraints on core temperatures. Earth Planet. Sci. Lett. 111 (2–4), 217–227.

Boehler, R., 1993. Temperatures in the Earth's core from melting-point measurements of iron at high static pressures. Nature 363 (6429), 534–536.

Boehler, R., Santamaría-Pérez, D., Errandonea, D., Mezouar, M., 2008. Melting, density, and anisotropy of iron at core conditions: new x-ray measurements to 150 GPa. J. Phys. Conf. Ser. 121, 022018. IOP Publishing.

Boehler, R., von Bargen, N., Chopelas, A., 1990. Melting, thermal expansion, and phase transitions of iron at high pressures. J. Geophys. Res., Solid Earth 95 (B13), 21731–21736.

Bower, D.J., Wicks, J.K., Gurnis, M., Jackson, J.M., 2011. A geodynamic and mineral physics model of a solid-state ultralow-velocity zone. Earth Planet. Sci. Lett. 303 (3–4), 193–202. http://www.sciencedirect.com/science/article/pii/S0012821X10008083.

Boyle, A.J.F., Bunbury, D.S.P., Edwards, C., Hall, H.E., 1961. The Mössbauer effect in tin from 120 °K to the melting point. Proc. Phys. Soc. 77 (1), 129. http://stacks.iop.org/0370-1328/77/i=1/a=316.

Brown, J.M., McQueen, R.G., 1986. Phase transitions, Grüneisen parameter, and elasticity for shocked iron between 77 GPa and 400 GPa. J. Geophys. Res., Solid Earth 91 (B7), 7485–7494. http://dx.doi.org/10.1029/JB091iB07p07485.

Brown, J.M., Shankland, T.J., 1981. Thermodynamic parameters in the Earth as determined from seismic profiles. Geophys. J. R. Astron. Soc. 66 (3), 579–596. http://dx.doi.org/10.1111/j.1365-246X.1981.tb04891.x.

Cacciamani, G., Dinsdale, A., Palumbo, M., Pasturel, A., 2010. The Fe–Ni system: thermodynamic modelling assisted by atomistic calculations. Intermetallics 18 (6), 1148–1162.

Chen, B., Li, J., Hauck, S.A., 2008. Non-ideal liquidus curve in the Fe–S system and Mercury's snowing core. Geophys. Res. Lett. 35 (7), L07201.

Corgne, A., Allan, N.L., Wood, B.J., 2003. Atomistic simulations of trace element incorporation into the large site of $MgSiO_3$ and $CaSiO_3$ perovskites. In: Diffusion and Partitioning in Planetary Interiors. Phys. Earth Planet. Inter. 139 (1–2), 113–127. http://www.sciencedirect.com/science/article/pii/S0031920103001481.

Deuss, A., 2014. Heterogeneity and anisotropy of Earth's inner core. Annu. Rev. Earth Planet. Sci. 42 (1), 103–126. http://dx.doi.org/10.1146/annurev-earth-060313-054658.

Dewaele, A., Loubeyre, P., Occelli, F., Mezouar, M., Dorogokupets, P.I., Torrent, M., 2006. Quasihydrostatic equation of state of iron above 2 Mbar. Phys. Rev. Lett. 97, 215504.

Dewaele, A., Mezouar, M., Guignot, N., Loubeyre, P., 2007. Melting of lead under high pressure studied using second-scale time-resolved x-ray diffraction. Phys. Rev. B 76, 144106.

Dewaele, A., Mezouar, M., Guignot, N., Loubeyre, P., 2010. High melting points of tantalum in a laser-heated diamond anvil cell. Phys. Rev. Lett. 104, 255701.

Dziewonski, A.M., Anderson, D.L., 1981. Preliminary reference Earth model. Phys. Earth Planet. Inter. 25 (4), 297–356.

Eng, P.J., Newville, M., Rivers, M.L., Sutton, S.R., 1998. Dynamically figured Kirkpatrick Baez x-ray microfocusing optics. SPIE Proceedings 3449, 145. http://dx.doi.org/10.1117/12.330342.

Errandonea, D., Schwager, B., Ditz, R., Gessmann, C., Boehler, R., Ross, M., 2001. Systematics of transition-metal melting. Phys. Rev. B 63, 132104.

Fei, Y., Bertka, C., 2005. The interior of Mars. Science 308 (5725), 1120–1121.

Fiquet, G., Auzende, A.L., Siebert, J., Corgne, A., Bureau, H., Ozawa, H., Garbarino, G., 2010. Melting of peridotite to 140 Gigapascals. Science 329 (5998), 1516–1518.

Fischer, R.A., Campbell, A.J., 2010. High-pressure melting of wüstite. Am. Mineral. 95 (10), 1473–1477.

Gao, L., Chen, B., Lerche, M., Alp, E.E., Sturhahn, W., Zhao, J., Yavas, H., Li, J., 2009. Sound velocities of compressed Fe_3C from simultaneous synchrotron X-ray diffraction and nuclear resonant scattering measurements. J. Synchrotron Radiat. 16 (6), 714–722.

Goncharov, A.F., Prakapenka, V.B., Struzhkin, V.V., Kantor, I., Rivers, M.L., Dalton, D.A., 2010. X-ray diffraction in the pulsed laser heated diamond anvil cell. Rev. Sci. Instrum. 81 (11), 113902. http://scitation.aip.org/content/aip/journal/rsi/81/11/10.1063/1.3499358.

Hier-Majumder, S., 2008. Influence of contiguity on seismic velocities of partially molten aggregates. J. Geophys. Res., Solid Earth 113 (B12), B12205. http://dx.doi.org/10.1029/2008JB005662.

Hirose, K., Labrosse, S., Hernlund, J., 2013. Composition and state of the core. Annu. Rev. Earth Planet. Sci. 41 (1), 657–691. http://dx.doi.org/10.1146/annurev-earth-050212-124007.

Hirschmann, M.M., Ghiorso, M.S., Wasylenki, L.E., Asimow, P.D., Stolper, E.M., 1998. Calculation of peridotite partial melting from thermodynamic models of minerals and melts. I. Review of methods and comparison with experiments. J. Petrol. 39 (6), 1091–1115. http://petrology.oxfordjournals.org/content/39/6/1091.abstract.

Jackson, J.M., Sturhahn, W., Lerche, M., Zhao, J., Toellner, T.S., Alp, E.E., Sinogeikin, S.V., Bass, J.D., Murphy, C.A., Wicks, J.K., 2013. Melting of compressed iron by monitoring atomic dynamics. Earth Planet. Sci. Lett. 362, 143–150.

Jeanloz, R., Heinz, D.L., 1984. Experiments at high temperature and pressure: laser heating through the diamond cell. J. Phys., Colloq. 45 (C8), 83–92.

Jeanloz, R., Kavner, A., 1996. Melting criteria and imaging spectroradiometry in laser-heated diamond-cell experiments. Philos. Trans. R. Soc., Math. Phys. Eng. Sci. 354 (1711), 1279–1305.

Kennett, B.L.N., Engdahl, E.R., Buland, R., 1995. Constraints on seismic velocities in the Earth from traveltimes. Geophys. J. Int. 122 (1), 108–124.

Komabayashi, T., 2014. Thermodynamics of melting relations in the system Fe–FeO at high pressure: implications for oxygen in the Earth's core. J. Geophys. Res., Solid Earth 119 (5), 4164–4177. http://dx.doi.org/10.1002/2014JB010980.

Komabayashi, T., Fei, Y., Meng, Y., Prakapenka, V., 2009. In-situ x-ray diffraction measurements of the γ–ϵ transition boundary of iron in an internally-heated diamond anvil cell. Earth Planet. Sci. Lett. 282 (1–4), 252–257.

Komabayashi, T., Hirose, K., Ohishi, Y., 2012. In situ X-ray diffraction measurements of the fcc–hcp phase transition boundary of an Fe–Ni alloy in an internally heated diamond anvil cell. Phys. Chem. Miner. 39 (4), 329–338.

Labrosse, S., Hernlund, J., Coltice, N., 2007. A crystallizing dense magma ocean at the base of the Earth's mantle. Nature 450 (7171), 866–869.

Labrosse, S., Poirier, J.-P., Mouël, J.-L.L., 2001. The age of the inner core. Earth Planet. Sci. Lett. 190 (3–4), 111–123. http://www.sciencedirect.com/science/article/pii/S0012821X01003879.

Lay, T., Garnero, E.J., Williams, Q., 2004. Partial melting in a thermo-chemical boundary layer at the base of the mantle. Phys. Earth Planet. Inter. 146 (3–4), 441–467. http://www.sciencedirect.com/science/article/pii/S0031920104002195.

Lay, T., Hernlund, J., Buffett, B.A., 2008. Core–mantle boundary heat flow. Nat. Geosci. 1 (1), 25–32.

Lehmann, I., 1936. P". Publ. Bur. Cent. Séismol. Int. A 14, S.87–S.115.

Li, J., Fei, Y., 2003. Experimental constraints on core composition. In: Treatise on Geochemistry, vol. 2, pp. 521–546.

Liu, L., Bassett, W.A., 1975. The melting of iron up to 200 kbar. J. Geophys. Res. 80 (26), 3777–3782.

Ma, Y., Somayazulu, M., Shen, G., Mao, H. Kwang, Shu, J., Hemley, R.J., 2004. In situ X-ray diffraction studies of iron to Earth-core conditions. In: New Developments in High-Pressure Mineral Physics and Applications to the Earth's Interior. Phys. Earth Planet. Inter. 143–144, 455–467. http://www.sciencedirect.com/science/article/pii/S0031920104000767.

Macedo, W.A.A., Keune, W., 1988. Magnetism of epitaxial fcc-Fe(100) films on Cu(100) investigated in situ by conversion-electron Mössbauer spectroscopy in ultrahigh vacuum. Phys. Rev. Lett. 61, 475–478. http://link.aps.org/doi/10.1103/PhysRevLett.61.475.

Mao, H.-K., Xu, J., Bell, P.M., 1986. Calibration of the ruby pressure gauge to 800-kbar under quasi-hydrostatic conditions. J. Geophys. Res. B, Solid Earth Planets 91 (B5), 4673–4676.

McDonough, W.F., Sun, S.-S., 1995. The composition of the Earth. Chem. Geol. 120 (3), 223–253.

McNamara, A.K., Garnero, E.J., Rost, S., 2010. Tracking deep mantle reservoirs with ultra-low velocity zones. Earth Planet. Sci. Lett. 299 (1–2), 1–9. http://www.sciencedirect.com/science/article/pii/S0012821X10004802.

Murphy, C.A., Jackson, J.M., Sturhahn, W., Chen, B., 2011. Melting and thermal pressure of hcp-Fe from the phonon density of states. Phys. Earth Planet. Inter. 188 (1–2), 114–120.

Nguyen, J.H., Holmes, N.C., 2004. Melting of iron at the physical conditions of the Earth's core. Nature 427 (6972), 339–342.

Ni, S., Helmberger, D.V., 2001. Probing an ultra-low velocity zone at the core mantle boundary with P and S waves. Geophys. Res. Lett. 28 (12), 2345–2348. http://dx.doi.org/10.1029/2000GL012766.

Nomura, R., Hirose, K., Uesugi, K., Ohishi, Y., Tsuchiyama, A., Miyake, A., Ueno, Y., 2014. Low core–mantle boundary temperature inferred from the solidus of pyrolite. Science 343 (6170), 522–525. http://www.sciencemag.org/content/343/6170/522.abstract.

Olson, P., 2013. The new core paradox. Science 342 (6157), 431–432. http://www.sciencemag.org/content/342/6157/431.short.

Poirier, J.-P., 2000. Introduction to the Physics of the Earth's Interior. Cambridge University Press.

Pradhan, G.K., Fiquet, G., Siebert, J., Auzende, A.-L., Morard, G., Antonangeli, D., Garbarino, G., 2015. Melting of {MORB} at core–mantle boundary. Earth Planet. Sci. Lett. 431, 247–255. http://www.sciencedirect.com/science/article/pii/S0012821X15006093.

Prescher, C., Prakapenka, V.B., 2015. Dioptas: a program for reduction of two-dimensional x-ray diffraction data and data exploration. High Press. Res. 35 (3), 223–230.

Rost, S., 2013. Deep Earth: core–mantle boundary landscapes. Nat. Geosci. 6 (2), 89–90.

Shen, G., Mao, H.-K., Hemley, R.J., Duffy, T.S., Rivers, M.L., 1998. Melting and crystal structure of iron at high pressures and temperatures. Geophys. Res. Lett. 25 (3), 373–376.

Shen, G., Prakapenka, V.B., Rivers, M.L., Sutton, S.R., 2004. Structure of liquid iron at pressures up to 58 GPa. Phys. Rev. Lett. 92, 185701.

Shen, G., Rivers, M.L., Wang, Y., Sutton, S.R., 2001. Laser heated diamond cell system at the Advanced Photon Source for in situ x-ray measurements at high pressure and temperature. Rev. Sci. Instrum. 72 (2), 1273–1282.

Singwi, K.S., Sjölander, A., 1960. Resonance absorption of nuclear gamma rays and the dynamics of atomic motions. Phys. Rev. 120, 1093–1102. http://link.aps.org/doi/10.1103/PhysRev.120.1093.

Stacey, F.D., 1977. A thermal model of the Earth. Phys. Earth Planet. Inter. 15 (4), 341–348. http://www.sciencedirect.com/science/article/pii/0031920177900966.

Stewart, A.J., Schmidt, M.W., van Westrenen, W., Liebske, C., 2007. Mars: a new core-crystallization regime. Science 316 (5829), 1323–1325.

Strong, H.M., Tuft, R.E., Hanneman, R.E., 1973. The iron fusion curve and γ–δ–l triple point. Metall. Trans. 4 (11), 2657–2661. http://dx.doi.org/10.1007/BF02644272.

Sturhahn, W., 2000. CONUSS and PHOENIX: evaluation of nuclear resonant scattering data. Hyperfine Interact. 125 (1–4), 149–172.

Sturhahn, W., 2015. MINUTI: open source software. http://www.nrixs.com.

Sturhahn, W., Jackson, J.M., 2007. Geophysical applications of nuclear resonant scattering. In: Advances in High-Pressure Mineralogy. In: GSA Special Paper, vol. 421. Geological Society of America, Boulder, Colorado, pp. 157–174.

Sun, D., Helmberger, D.V., Jackson, J.M., Clayton, R.W., Bower, D.J., 2013. Rolling hills on the core–mantle boundary. Earth Planet. Sci. Lett. 361 (0), 333–342. http://www.sciencedirect.com/science/article/pii/S0012821X12005961.

Tateno, S., Hirose, K., Ohishi, Y., 2014. Melting experiments on peridotite to lowermost mantle conditions. J. Geophys. Res., Solid Earth 119 (6), 4684–4694. http://dx.doi.org/10.1002/2013JB010616.

Terasaki, H., Kamada, S., Sakai, T., Ohtani, E., Hirao, N., Ohishi, Y., 2011. Liquidus and solidus temperatures of a Fe–O–S alloy up to the pressures of the outer

core: implication for the thermal structure of the Earth's core. Earth Planet. Sci. Lett. 304 (3), 559–564.

Thomas, C.W., Asimow, P.D., 2013. Direct shock compression experiments on premolten forsterite and progress toward a consistent high-pressure equation of state for CaO–MgO–Al_2O_3–SiO_2–FeO liquids. J. Geophys. Res., Solid Earth 118 (11), 5738–5752. http://dx.doi.org/10.1002/jgrb.50374.

Thorne, M.S., Garnero, E.J., Jahnke, G., Igel, H., McNamara, A.K., 2013. Mega ultra low velocity zone and mantle flow. Earth Planet. Sci. Lett. 364, 59–67. http://www.sciencedirect.com/science/article/pii/S0012821X12007200.

Toellner, T.S., 2000. Monochromatization of synchrotron radiation for nuclear resonant scattering experiments. Hyperfine Interact. 125 (1–4), 3–28.

Wicks, J.K., Jackson, J.M., Sturhahn, W., 2010. Very low sound velocities in iron-rich (Mg, Fe)O: implications for the core–mantle boundary region. Geophys. Res. Lett. 37 (15). http://dx.doi.org/10.1029/2010GL043689.

Williams, Q., Garnero, E.J., 1996. Seismic evidence for partial melt at the base of Earth's mantle. Science 273 (5281), 1528–1530. http://www.sciencemag.org/content/273/5281/1528.abstract.

Williams, Q., Jeanloz, R., Bass, J., Svendsen, B., Ahrens, T.J., 1987. The melting curve of iron to 250 Gigapascals – a constraint on the temperature at earths center. Science 236 (4798), 181–182.

Yoo, C.S., Holmes, N.C., Ross, M., Webb, D.J., Pike, C., 1993. Shock temperatures and melting of iron at Earth core conditions. Phys. Rev. Lett. 70, 3931–3934.

Zhang, D., Jackson, J.M., Zhao, J., Sturhahn, W., Alp, E.E., Toellner, T.S., Hu, M.Y., 2015. Fast temperature spectrometer for samples under extreme conditions. Rev. Sci. Instrum. 86, 013105.

Zhao, J., Sturhahn, W., Lin, J.-F., Shen, G., Alp, E.E., Mao, H.-K., 2004. Nuclear resonant scattering at high pressure and high temperature. High Press. Res. 24 (4), 447–457.